ELSEVIER

Journal of Power Sources 112 (2002) 298–306

JOURNAL OF POWER SOURCES

www.elsevier.com/locate/jpowsour

An experimental and modeling study of isothermal charge/discharge behavior of commercial Ni–MH cells

Y.H. Pan, V. Srinivasan, C.Y. Wang*

Electrochemical Engine Center, and Department of Mechanical and Nuclear Engineering, The Pennsylvania State University, University Park, PA 16802, USA

Received 5 July 2002; accepted 20 July 2002

Abstract

In this study, a previously developed nickel–metal hydride (Ni–MH) battery model is applied in conjunction with experimental characterization. Important geometric parameters, including the active surface area and micro-diffusion length for both electrodes, are measured and incorporated in the model. The kinetic parameters of the oxygen evolution reaction are also characterized using constant potential experiments. Two separate equilibrium equations for the Ni electrode, one for charge and the other for discharge, are determined to provide a better description of the electrode hysteresis effect, and their use results in better agreement of simulation results with experimental data on both charge and discharge. The Ni electrode kinetic parameters are re-calibrated for the battery studied. The Ni–MH cell model coupled with the updated electrochemical properties is then used to simulate a wide range of experimental discharge and charge curves with satisfactory agreement. The experimentally validated model is used to predict and compare various charge algorithms so as to provide guidelines for application-specific optimization.

Keywords: Ni–MH battery; Mathematical model; Oxygen evolution reaction; Coupled characterization and modeling

1. Introduction

The nickel–metal hydride (Ni–MH) battery is an attractive replacement for the Ni–Cd battery due to its high energy density, high rate capability, long cycle life and lack of poisonous materials. The demand for nickel–metal hydride batteries has recently grown for applications ranging from portable electrics to electric and hybrid-electric vehicles. For clean transportation, Ni–MH battery is presently the most promising battery for hybrid-electric vehicles based on the performance and cost. Extensive efforts have been made to develop various advanced nickel–metal hydride batteries to meet commercial requirements.

Traditionally, experimental testing is a main tool to test and design batteries. However, experiments are time consuming and costly, and experimentally it is difficult to determine the internal process during charge and discharge. Modeling and simulation of batteries is a useful method for battery designers because a good cell model can be used to identify battery mechanisms, predict the cell performance for design and optimization, and reduce the cost and time expended on the experiments.

Several models have been developed to study the nickel electrode [1–5,13], metal hydride electrode [6–9] as well as the complete nickel–metal hydride battery [10,12,13]. Vidts and White [4] developed a pseudo-2D mathematical model of a sealed nickel–cadmium cell including proton diffusion and ohmic drop in the nickel electrode. In addition, the oxygen evolution reaction was coupled with main electrochemical reactions on both electrodes. A sensitivity analysis was performed to determine the effects of various parameters in the model. They found that at the beginning of discharge, the sensitivity of exchange current density of the reduction of NiO(OH) is the largest; as the discharge proceeds, the sensitivity coefficient of the transfer coefficient of the reduction of NiO(OH) becomes the largest gradually; the effect of diffusion coefficient of proton on the discharge efficiency is the largest at higher discharge rates. In their work, however no experimental data was used to verify the model.

Paxton and Newman [10] developed a nickel–metal hydride cell model using new data on the diffusion coefficient of proton in the nickel active materials as measured by Motupally et al. [11]. In this model, the open-circuit

* Corresponding author. Tel.: +1-814-863-4762; fax: +1-814-863-4848.
E-mail address: cxw31@psu.edu (C.Y. Wang).

0378-7753/02/$ – see front matter
PII: S0378-7753(02)00450-0

potentials for both electrodes were experimentally measured as functions of the state of charge. They argued that the proton diffusion could be neglected in the low rate range they studied. They showed that during discharge, the potential drop at the nickel electrode is the largest loss of the nickel–metal hydride cell. Some experimental discharge curves from three different cells running at the 0.5 C discharge were compared with their model, but poor agreement can be seen due to a lack of most physico-chemical properties for the cells. The oxygen evolution reaction was not included.

A three-phase electrochemical model was developed by Gu et al. [12] for nickel–metal hydride cells using the micro-macroscopic coupled approach. By including the oxygen reaction in the cell, the effect of oxygen evolution on the cell voltage was assessed, in particular, the charge acceptance is correlated with the charge rate and the evolution of oxygen is responsible for the cell pressure build-up. In addition, they compared experimental data and modeling results for different rate charge and discharge processes; however, the agreement was not satisfactory in general for various charge and discharge rates.

The objective of this research is three-fold: (1) to produce benchmark experimental data with all needed physico-chemical properties that will be useful for all model validation exercises; (2) to refine the first-principles mathematical model of Gu et al. [12] to more accurately describe the behavior of commercial Ni–MH cells under a wide range of operating conditions, particularly constant current (CC) charge and discharge, and constant voltage (CV) operation; and (3) to provide some design change examples for optimizing the performance of the battery using the validated model.

2. Model development

The nickel–metal hydride battery consists a Ni positive electrode and a MH negative electrode. During the discharge and charge processes, the electrochemical reactions taking place at both electrodes are given by:

Negative electrode

$$\mathrm{MH} + \mathrm{OH}^- \underset{\text{charge}}{\overset{\text{discharge}}{\Leftrightarrow}} \mathrm{H_2O} + \mathrm{e}^- \tag{1}$$

with the side reaction

$$\tfrac{1}{2}\mathrm{O_2} + \mathrm{H_2O} + 2\mathrm{e}^- \rightarrow 2\mathrm{OH}^- \tag{2}$$

$$\mathrm{H_2} + 2\mathrm{OH}^- \rightarrow 2\mathrm{H_2O} + 2\mathrm{e}^- \tag{3}$$

Positive electrode

$$\mathrm{NiOOH} + \mathrm{H_2O} + \mathrm{e}^- \underset{\text{charge}}{\overset{\text{discharge}}{\Leftrightarrow}} \mathrm{Ni(OH)_2} + \mathrm{OH}^- \tag{4}$$

with the side reaction

$$\mathrm{OH}^- \rightarrow \tfrac{1}{2}\mathrm{O_2} + \mathrm{H_2O} + \mathrm{e}^- \tag{5}$$

$$2\mathrm{H_2O} + 2\mathrm{e}^- \rightarrow \mathrm{H_2} + 2\mathrm{OH}^- \tag{6}$$

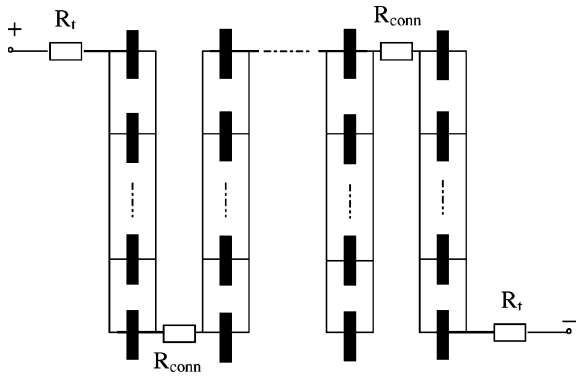

Fig. 1. Schematic configuration of a battery module.

For these electrochemical reactions, we follow the derivation of Vidts and White [4] and Vidts et al. [6]. Both liquid and solid phases are involved in species transfer during charge and discharge processes, and O_2 transport in the gas and liquid phases is considered. Charge conservation equations are applied to both solid and liquid phases. From these conservation equations the solid and liquid phase potentials can be determined. The model used in this paper is identical to that of Gu et al. [12] and hence is not repeated herein.

A battery module as schematically shown in Fig. 1 is composed of many cells connected in series, as well as in parallel. The module modeling can be approached by considering cells to be connected in series and in parallel as well as resistances of inter-cell and terminals. The battery module voltage can thus be related to the cell voltage by the following:

$$V_s = \sum_{j=1}^{N_s} V_c^j - \sum_{j=1}^{N_s-1} I_s R_{conn}^j - \sum_{j=1}^{2} I_s R_t^j \tag{7}$$

where N_s is the number of cell in series, I_s is the current flowing through the battery stack, R_{conn}^j is the j-th connector resistance and R_t^j is the j-th terminal resistance. Assuming that all cells in the module behave identically, the cell voltage, $V_c^j \equiv V_c$, can thus be expressed as:

$$V_c = \frac{1}{N_s}[V_s + (N_s - 1)R_{conn}I_s + 2R_tI_s] \tag{8}$$

Here, V_c is the common voltage of single cells.

3. Numerical procedure

As elaborated in Gu et al. [12], all equations in this model are discretized by the finite volume method and solved by a general-purpose computation fluid dynamic (CFD) code. The initial condition is set according to the initial state of charge (SOC) and species concentrations. The boundary condition depends on the charge/discharge mode. The size of a finite volume is about 1/20 of an electrode thickness. A typical discharge simulation requires about 5 min of CPU time on a PC with 450 MHz CPU.

4. Experimental

All experiments are performed on a commercial nickel–metal hydride battery of nominal capacity 95 Ah, which consists of ten cells in series. Experiments were performed with a computer-controlled battery testing system (Arbin Instruments). To keep the isothermal conditions, fans have been used to induce forced convection, and the variations of temperature were determined to be within 5 °C by thermocouples placed on the surface of the tested batteries. The same charge process was used for all discharge experiments: 20 A CC step until the battery voltage reaches 14.35 V, followed by a CV step until the charge capacity reaches 100 Ah, finally rests for 1 h after each full charge. The discharge cutoff voltage for all low rates is 10.5 V, but this is lowered to 10.0, 9.5, and 8.0 V for 1, 2, and 3 C-rates, respectively. For all charge experiments, fully discharge the battery by constant 0.1 C-rate until the cutoff voltage of 10.5 V. During charge, the cutoff voltage was set at 15 V at high rates, and at low rates batteries were allowed to reach the maximum voltage.

5. Results and discussion

5.1. Experiment data

5.1.1. Reproducibility of battery data

The mathematical model is developed to predict and simulate the behavior of a single cell. Therefore, only when the variations among the cells in a battery module were small enough, the simulation could be used to predict the battery performance and direct its design. Fig. 2 shows the constant current discharge curve and error bars for different cells at 0.2 C-rate discharge. It is obvious that the performances of different cells are quite similar. Therefore, it is reasonable to use the cell model, which assume that each cell has the same behavior as others, to simulate an entire battery and predict its behaviors.

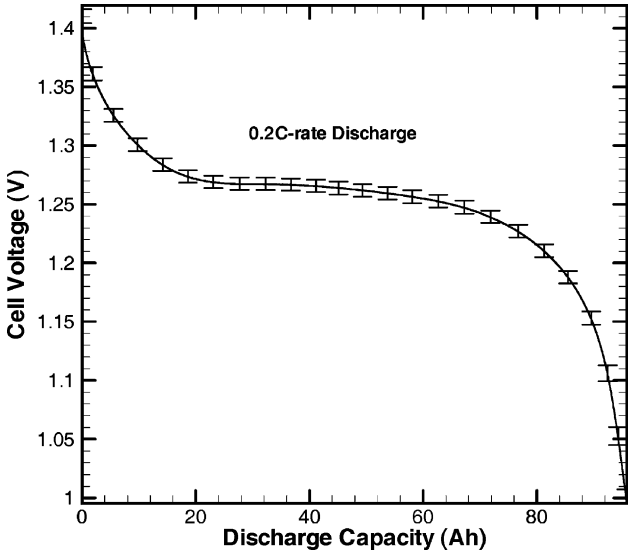

Fig. 2. Reproducibility of cell data during discharge.

5.1.2. Determination of the surface area of electrode

The surface areas of both electrodes are determined by BET method; for the Ni electrode, it has a BET surface area of 26.5 m^2/g, and for the MH electrode, it has a surface area of 1.9 m^2/g. The specific surface area of each electrode, a_0, can be expressed by:

$$a_0 = \rho S \tag{9}$$

where S is the BET surface area and ρ the density of each electrode. Assuming that all particles are spherical, thus the total solid volume is given by:

$$V_s = V(1 - \varepsilon_0) = \tfrac{4}{3} n\pi r^3 \tag{10}$$

The total solid surface area, s is expressed by:

$$s = 4\pi n r^2 \tag{11}$$

Therefore, the surface area a_0 can be related to porosity and the radius of particles by the following equation:

$$a_0 = \frac{s}{V_s} = \frac{3(1 - \varepsilon_0)}{r} \tag{12}$$

Assume a known porosity, the equivalent radius can be determined from the above equation. All geometrical parameters that are different from those in Gu et al. [12] are now listed in Table 1.

5.1.3. Oxygen evolution

It is known that the effect of oxygen reaction is important at the late stage of charge. In order to describe the oxygen reaction accurately, constant potential experiment is carried out, in which the battery is first charged at C/4 rate until a sufficiently high potential to ensure nearly full charge, and subsequently the potential is held steady

Table 1
Cell geometrical parameters

Parameter	Value	Unit
Ni electrode		
Thickness	0.045	cm
Projected electrode area	14 × 11	cm^2
r_{Ni}	784000	cm^2/cm^3
ε_{Ni}	0.33	
a_{Ni}	1.56×10^{-4}	cm
Separator		
Thickness	0.017	cm
MH electrode		
Thickness	0.029	cm
a_{MH}	57490	cm^2/cm^3
ε_{MH}	0.52	
r_{MH}	2.5×10^{-5}	cm

until the charge current reaches a steady value. This current can be considered as the oxygen reaction current. Due to the small transfer current density, it is suitable to assume that all concentration distributions within the battery are uniform, and that the ohmic drop as compared to the kinetic polarization within the porous electrode is small, namely, the potential distribution within the electrode is uniform. Based on these assumptions, Tafel equation can be used to describe oxygen evolution reaction as shown below:

$$\eta = a + b\log(i) \tag{13}$$

where η is the overpotential of the oxygen evolution reaction and i the true reaction current density of the oxygen reaction, which can be calculated by:

$$i = \frac{i_s}{a_0 l} \tag{14}$$

Here i_s is the superficial current density, i.e.

$$i_s = \frac{I}{A} \tag{15}$$

l is the thickness of the Ni electrode, I is the total current passing through the battery, and A is the projected surface area of the Ni electrode. The values of a and b are found in Fig. 3. If the ohmic drop cannot be neglected or the concentration distribution is not uniform, porous electrode theory [14] should be used instead. From the following two equations:

$$a = -\frac{2.3RT}{\alpha_a F}\log i_0 \tag{16}$$

$$b = \frac{2.3RT}{\alpha_a F} \tag{17}$$

the exchange current density of oxygen evolution reaction, $i_0 = 7.83 \times 10^{-15}$ A/cm^2, and the transfer coefficient of anode reaction, $\alpha_a = 1.5$, are found.

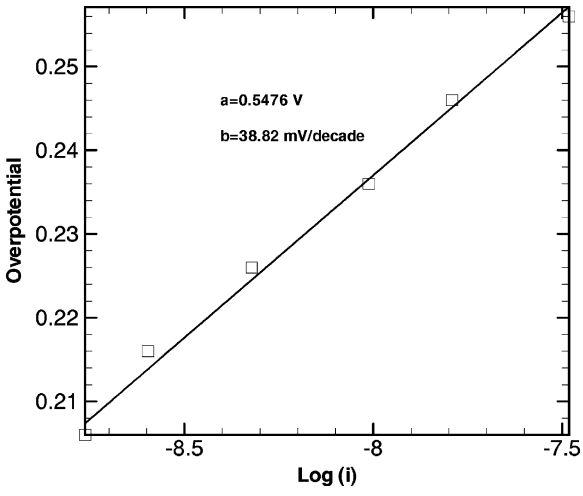

Fig. 3. Tafel plot of oxygen evolution reaction.

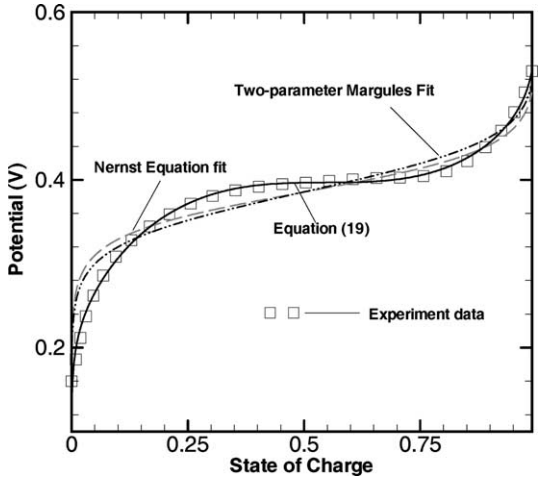

Fig. 4. Comparison of different equilibrium potentials.

5.2. Model-experimental comparisons

The difference between the predicted cell open-circuit potential and experimental data is clearly seen in Fig. 4, where the low rate (0.05 C-rate) data is compared to various thermodynamic expressions. Note that Fig. 4 assumes that a low rate experiment can be used to approximate the equilibrium potential of the cell as a function of SOC. In other words, it is assumed that kinetic, ohmic, mass transfer losses and self-discharge due to oxygen evolution can be neglected under such rate.

In the Ni–MH battery system, the capacity of MH electrode is much larger than that of Ni electrode due to the overcharge and overdischarge reserve. Therefore, the state of charge of the MH potential usually stays at the middle part. According to Haran et al.'s [8] experimental data, the equilibrium potential of MH electrode in this part is nearly constant. Thus, during discharge/charge the MH potential can be assumed constant at low rates (0.05 C-rate for discharge and 0.1 C-rate for charge). Accounting for the intercalation in the Ni electrode, a one-parameter Margules model was used in Gu et al. [12] to correct the activity of proton. A two-parameter Margules expression correcting Nernst equation for Ni electrode is also shown in Fig. 4, which can be expressed as:

$$E^0 = 0.3854 + \frac{1}{38.94}\ln\left(\frac{x}{1-x}\right) + \frac{1}{19.97}(2\times 0.8186 - 0.8186\times 4(1-x) - 2\times 0.9498 + 6\times 0.9498(1-x) - 3\times 0.9498(1-x)^2) \tag{18}$$

where E^0 is the equilibrium potential of the Ni electrode and x is the state of charge. It can be seen that the two-parameter Margules model makes the curve flatter than the one predicted by Nernst equation. However, the slope of the curve at intermediate SOC is much steeper than that seen experimentally, and it still cannot capture the main shape of the

equilibrium potential curve. Considering the inability of these theoretical models to fit the data, the data was curve-fitted to the following equation:

$$E^0 = 0.314 + \frac{1}{38.94} \times \ln\left(\frac{x}{1-x}\right) + 0.5997x - 1.1889x^2 + 0.5937x^3 + 0.0985x^4 \quad (19)$$

This expression is subsequently employed in the mathematical model.

According to Paxton and Newman [10] and Gu et al.'s [12] work, the proton diffusion would not be important if the proton diffusion length is small. The length measured in this work is substantially smaller than the length used by Gu et al. [12]. Therefore, the present diffusion coefficient of proton is the same as Gu et al. [12], measured by MacArthur [15].

From Paxton and Newman's [10] discussion, the parameters of the nickel electrode affect the battery discharge behavior most. Thus, we fit the highest rate discharge curve to obtain a more realistic set of kinetic parameters of Ni electrode. Table 2 shows new kinetic parameters used in the corresponding simulation study. Note that the product of the specific surface area and exchange current density used in the present work is only slightly different from the value used by Gu et al. [12] for the Ni electrode and is exactly the same for the MH electrode. In addition, the transfer coefficient, α, which affects the shape of the discharge curve of Ni electrode, is another parameter adjusted for better agreement with the experimental data.

Fig. 5 displays a comparison between experimental and simulated discharge curves over a wide range of C-rates. It can be seen that the main shapes of the experimental discharge curves were captured successfully by the simulation. Especially at 0.1 C-rate, even the initial quick drop in the cell potential was predicted well, showing that at low rate discharge Nernst equation controls the behavior of the battery. At the middle part, all predictions are in good agreement with the measured curves. It can be found that the prediction of battery capacity is fairly accurate at all rates. Changing the diffusion coefficient in the model does not affect the discharge curve, thus indicating that the proton transport is not a limiting step, in accordance with the observations of Paxton and Newman [10] and Gu et al. [12]. In summary, the present Ni–MH model coupled with the well-characterized kinetic and transport properties results in generally satisfactory agreement with discharge data over a wide range of rates.

Due to the hysteresis effect on Ni electrode, the open-circuit potential equation for both discharge and charge processes may not be the same. Because of oxygen evolution reaction during the charge process, which can significantly affect the end part of the charge process, we cannot use the same method as for discharge to determine the open-circuit equilibrium potential of the charge process. Instead, we use the same formula as the discharge part, but slightly adjust the coefficients to obtain the charge open-circuit potential of Ni electrode as follows (also shown in Fig. 6):

$$E^0 = 0.494 + \frac{1}{38.94} \times \ln\left(\frac{x}{1-x}\right) + 0.07841x - 0.224424x^2 + 0.044965x^3 + 0.044965x^4 \quad (20)$$

With the above open-circuit potential for charge but otherwise all the same physico-chemical properties as for discharge,

Table 2
Kinetic parameters for Ni electrode

Parameter	Present paper	Gu et al. [12]	Unit
α_a^{Ni}	0.73	0.5	
α_c^{Ni}	0.27	0.5	
ai_0^{Ni}	0.4666	0.4194[a]	A/cm^3

[a] Obtained from individual values of a and i_0^{Ni} listed in Gu et al. [12].

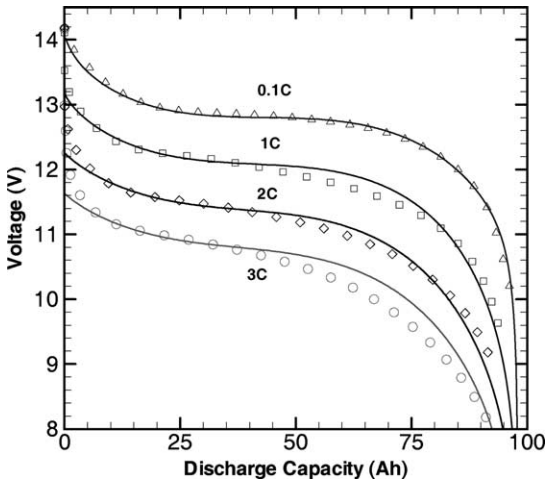

Fig. 5. Comparison of simulated battery voltages (solid lines) with experimental data (symbols).

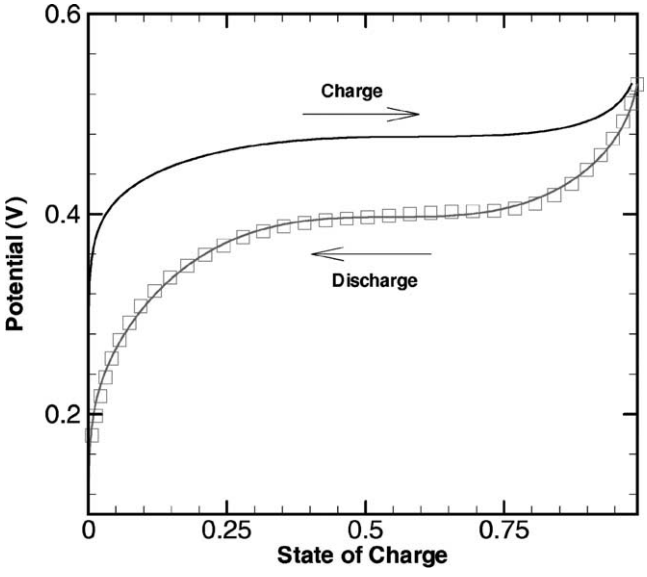

Fig. 6. Open-circuit potential of Ni electrode with respect to state of charge (solid lines for model and symbols for experimental data).

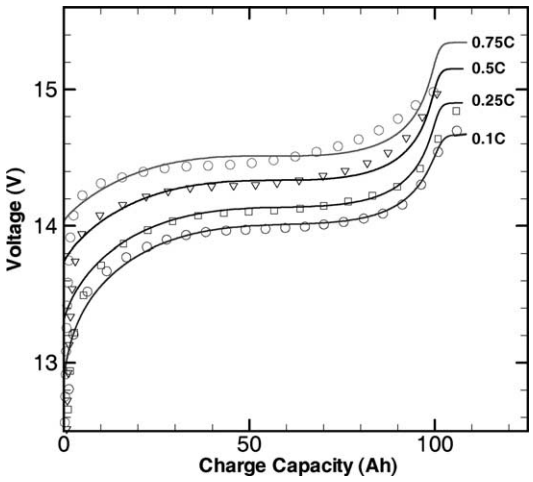

Fig. 7. Comparison of simulation battery voltages (solid lines) with experimental data (symbols).

Fig. 7 displays a comparison of the simulated and measured charge curves over a range of C-rates. It can be seen that the simulations agree well with the experimental data. From the plot, we can see that at the beginning of charge, the potentials for all rates increase fast, then become nearly constant until 90 Ah, followed by a steep increase again near full charge, and lastly a constant plateau due to the balance of oxygen evolution and recombination reactions within the battery. It is interesting to observe that the plateau of each curve in overcharge occurs almost at the same charge capacity. This seems to suggest that the oxygen cycle does not start until full charge.

From the model, one can conveniently calculate the respective distributions of the main reaction and oxygen evolution reaction currents. It can be seen from Fig. 8 that the side reaction current is relatively small before the charge capacity reaches 85 Ah for all rates charge. After that the side reaction rate increases sharply until reaching the total charge current. Charging beyond 102 Ah, nearly the entire charge current for all rates is to supply the oxygen reaction.

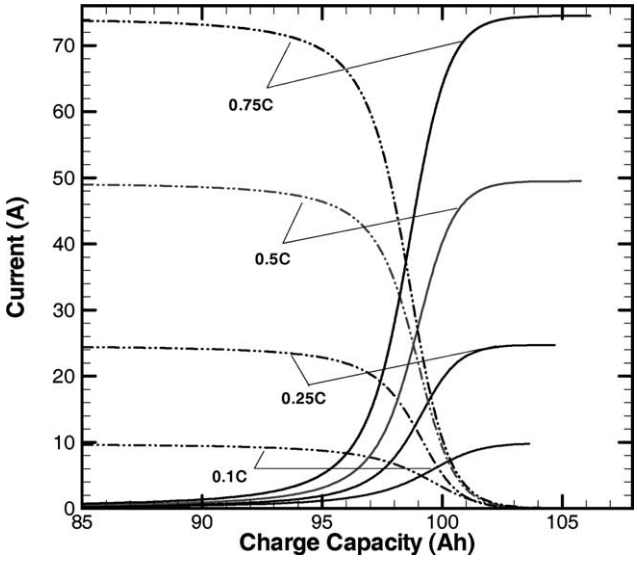

Fig. 8. Comparison of oxygen reaction current (dashed lines) and main reaction current (solid lines) for various C-rates during charge.

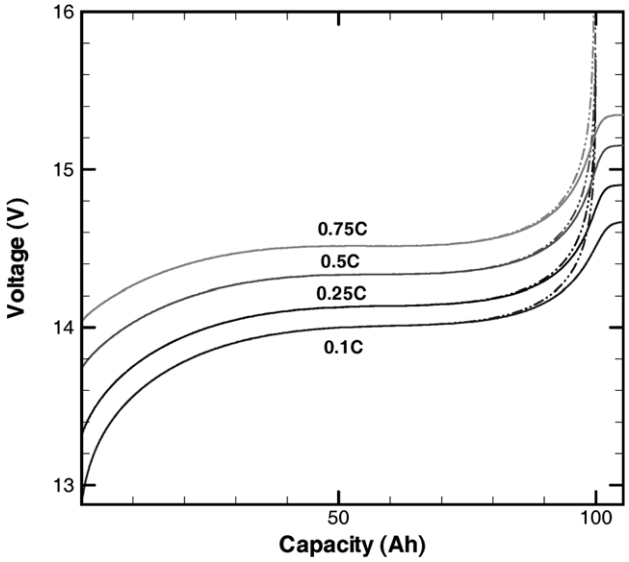

Fig. 9. Comparison of battery charge curves with (solid lines) and without oxygen reaction (dashed lines).

Fig. 9 shows the predicted effects of oxygen reaction on the charge potential. During charge, most part of the charge curve is not affected by oxygen reaction, in consistency with Fig. 8. It is interesting that oxygen side reaction affects charge potential at low rates much more than at high rates. This is the main reason why it is not suitable to consider the low rate charge curve as the equilibrium potential due to the oxygen evolution.

5.3. Battery design

The charge algorithm is an important part of battery applications, especially for electric and hybrid electric vehicles, because it is desirable to charge the battery in the shortest time and at the highest charge efficiency. However, both goals cannot be achieved simultaneously because the parasitic current associated with oxygen reaction increases with charge rate and state of charge. Charge algorithms are typically optimized by experimental trial-and-error. Using a validated model to assist in this optimization can be a cost-effective alternative.

Charge algorithms typically consist either of a constant current step, or of a constant current step followed by a constant voltage step. Fig. 10 displays the latter method for the 12 V Ni–MH battery and shows the final state of charge and charge efficiency as functions of the voltage step level. The charge efficiencies for all charge rates decrease with the final voltage level, due to the side reactions having more effect at higher potentials. The final SOC is solely determined by the voltage level, regardless of the rate of current used in the first step, and increases with the voltage level.

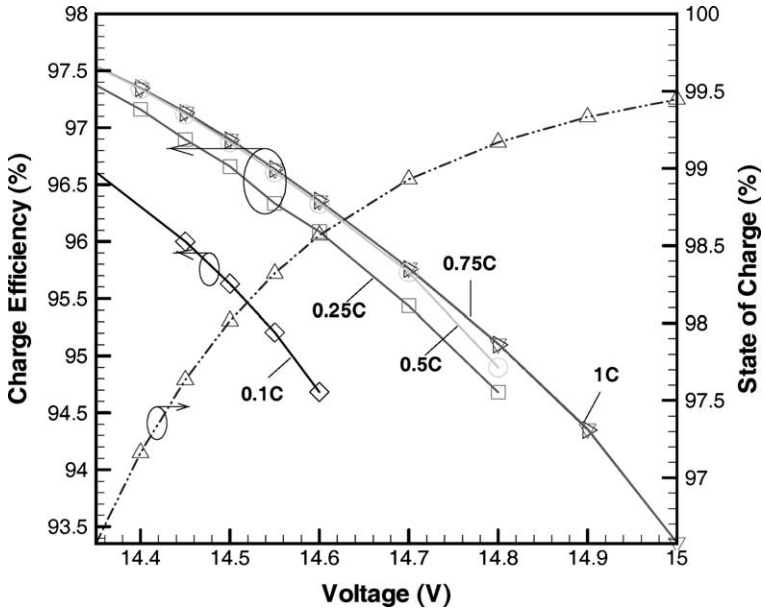

Fig. 10. Charge efficiency (solid lines) and final state of charge (dashed lines) for a 12 V Ni–MH battery by constant current followed by constant voltage method.

The charge efficiency shows the opposite trend; the efficiency decreases at a certain C-rate as the voltage level is increased. On the other hand, the figure shows that the charge efficiency increases with charge rate at a certain charge voltage. This increase is shown more clearly in Fig. 11, which further indicates that the charge efficiency becomes nearly constant above 0.5 C. It is evident from the discussion above that low rate charging, e.g. 0.1 C, up to a particular constant voltage level is not desirable due to the low charge efficiency. A compromise between these competing effects must be made to determine the optimum algorithm.

Fig. 12 shows the charge efficiency with respect to the charge input for constant current charge method. The charge efficiency increases with the charge rate and then reaches a maximum between 0.5 and 1 C. The efficiency decreases with charge rates above 1 C. The charge efficiency is high at the beginning of charge for low charge rates (e.g. <0.25 C), but then decreases quickly with the charge input. It is interesting that the charge efficiency at low charge rates for constant current charging is lower than for higher rates. These observations show that charge rates near 1 C are optimal for achieving maximum charge efficiency.

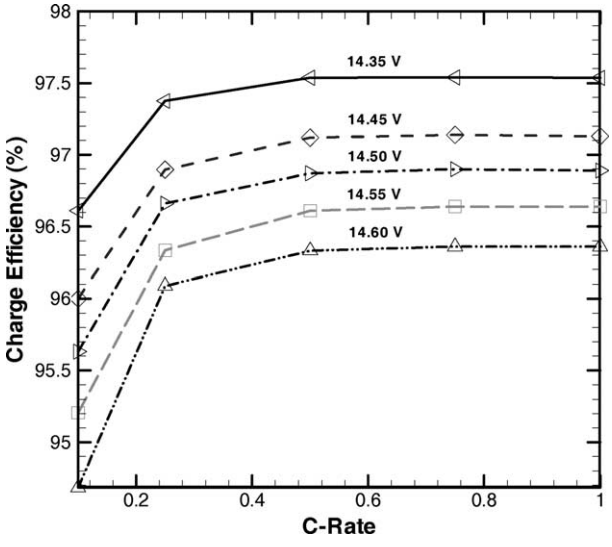

Fig. 11. Charge efficiency as a function of C-rate by constant current followed by constant voltage method.

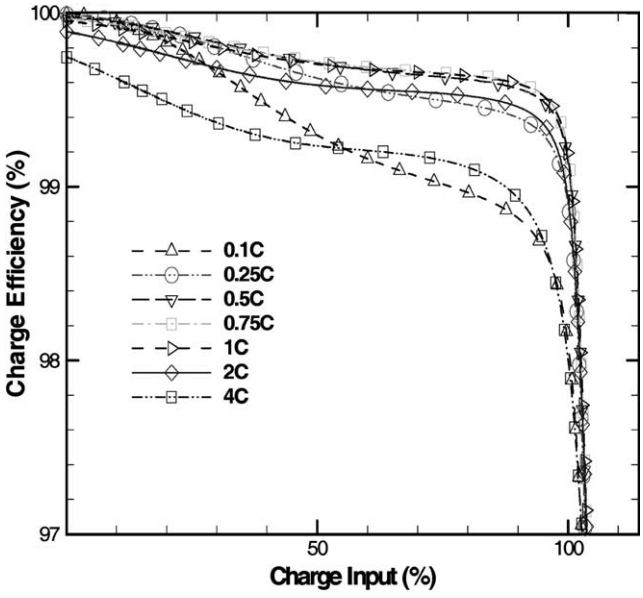

Fig. 12. Charge efficiency of battery at different constant charge rates.

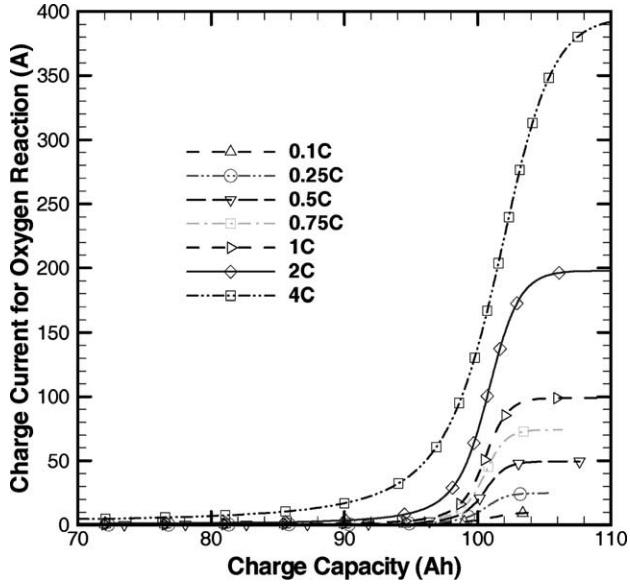

Fig. 13. Parasitic current of oxygen reaction at different constant charge rates.

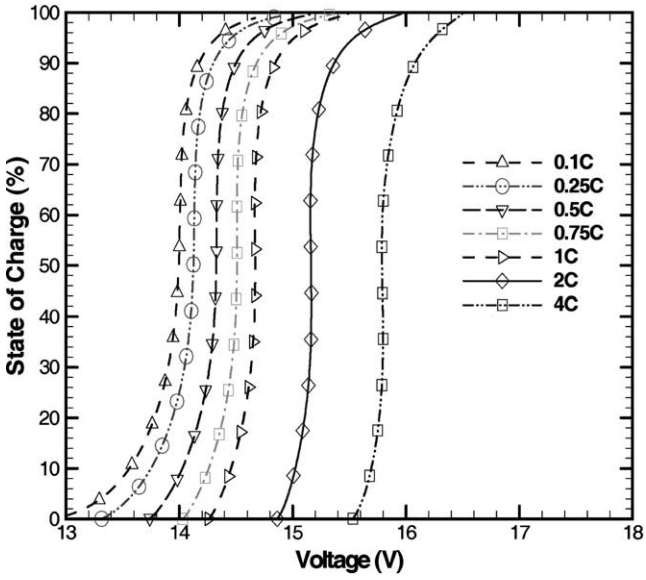

Fig. 15. The final state of charge as a function of the terminating voltage in constant current charge.

Fig. 13 displays the oxygen reaction current with respect to charge input for different charge rates. As expected, larger charge rates result in higher side reaction currents. This result seems to suggest that the charge efficiency decreases with the increase of charge rate due to the larger side reaction current at the higher charge rate. However, the charge time is also different for different rates, and the total charge capacity that goes into the side reaction is determined by the product of time and current. The charge capacity consumed by the side reaction at different charge rates with respect to charge input is plotted in Fig. 14. The side reaction charge capacity is the lowest at intermediate charge rates, with the highest for both 0.1 and 4 C, which agrees with the conclusion drawn from Fig. 12.

Fig. 15 shows the relationship between the final state of charge and the terminating battery voltage during constant current charging. The relationship for all charge rates exhibits the same trend: initially the state of charge increases gradually, followed by a sharp increase, and then tails off as the SOC approaches 100%. The charge efficiency for a given charge rate, however, decreases with the terminating voltage as shown in Fig. 16. The main reaction charge efficiency drops off sharply as the cell potential approaches a certain value because the charge current is used dominantly in the oxygen cycle. Figs. 15 and 16 can be used to determine the cutoff voltage of constant current charge algorithm according to the desired charge efficiency and state of charge.

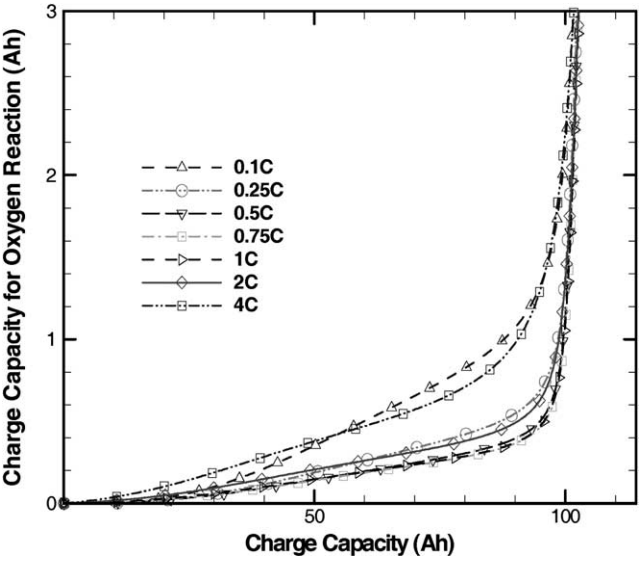

Fig. 14. Charge capacity consumed by the oxygen reaction for different charge rates.

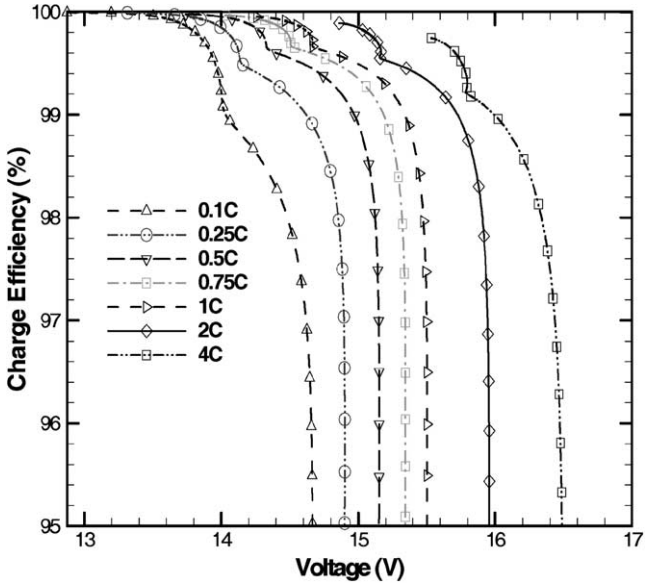

Fig. 16. Charge efficiency vs. final voltage for constant current charge.

6. Conclusion

An approach to closely coupling modeling with experimentation has been attempted for a commercially available Ni–MH battery. The battery parameters, the equilibrium potential of the Ni electrode and its hysteresis effect, and the kinetics of oxygen reaction were characterized and incorporated into a previously developed first-principles model to result in a generally good agreement between experimental and predicted discharge as well as charge curves. The validated mathematical model was then used to study charge algorithms. Low rate charging is not desirable due to the lower charge efficiency for both charge algorithms: the constant current step and the constant current step followed by constant voltage step. The model predictions show that 1 C-rate charge can be used to quickly charge the battery, while still achieving the highest charge efficiency. Future work will concentrate on the thermal effects in Ni–MH batteries.

Acknowledgements

Financial support from DOT Advanced Vehicle Program under cooperative agreement no. DTRS56-99-T-0016 is gratefully acknowledged.

References

[1] D. Fan, R.E. White, J. Electrochem. Soc. 138 (1991) 17–25.
[2] D. Fan, R.E. White, J. Electrochem. Soc. 138 (1991) 2952–2960.
[3] Z. Mao, P.D. Vidts, R.E. White, J. Newman, J. Electrochem. Soc. 141 (1994) 54–64.
[4] P.D. Vidts, R.E. White, J. Electrochem. Soc. 142 (1995) 1509–1519.
[5] B.V. Ratnakumar, P. Timmerman, C. Sanchez, S.D. Stefano, G. Halpert, J. Electrochem. Soc. 143 (1996) 803–812.
[6] P.D. Vidts, J. Delgado, R.E. White, J. Electrochem. Soc. 142 (1995) 4006–4013.
[7] J.M. Heikonen, H.J. Ploehn, R.E. White, J. Electrochem. Soc. 145 (1998) 1840–1848.
[8] B.S. Haran, B.N. Popov, R.E. White, J. Electrochem. Soc. 145 (1998) 4082–4089.
[9] V.R. Subramanian, H.J. Ploehn, R.E. White, J. Electrochem. Soc. 147 (2000) 2868–2873.
[10] B. Paxton, J. Newman, J. Electrochem. Soc. 144 (1997) 3818–3830.
[11] S. Motupally, C. Streinz, J. Weidner, J. Electrochem. Soc. 142 (1995) 1401–1408.
[12] W.B. Gu, C.Y. Wang, S.M. Li, M.M. Geng, B.Y. Liaw, Electrochim. Acta 44 (1999) 4525–4541.
[13] C.Y. Wang, W.B. Gu, B.Y. Liaw, J. Electrochem. Soc. 145 (1998) 3407–3417.
[14] L.G. Austin, Trans. Faraday Soc. 60 (1964) 1319–1324.
[15] D.M. MacArthur, J. Electrochem. Soc. 117 (1970) 729–733.